catalysts

MDPI

Article

Dehydrogenation of 2-[(*n*-Methylcyclohexyl)Methyl]Piperidine over Mesoporous Pd-Al_2O_3 Catalysts Prepared by Solvent Deficient Precipitation: Influence of Calcination Conditions

Hari Babu Bathula [1,2,†], Jinho Oh [1,†], Yeongin Jo [1] and Young-Woong Suh [1,2,*]

1 Department of Chemical Engineering, Hanyang University, Seoul 04763, Korea
2 Research Institute of Industrial Science, Hanyang University, Seoul 04763, Korea
* Correspondence: ywsuh@hanyang.ac.kr
† The authors contributed equally to this work.

Received: 24 July 2019; Accepted: 22 August 2019; Published: 26 August 2019

Abstract: A pair of 2-[(*n*-methylcyclohexyl)methyl]piperidine (H_{12}-MBP) and its full dehydrogenation product (H_0-MBP) has recently been considered as a potential liquid organic hydrogen carrier with 6.15 wt% H_2 storage capacity. In the discovery of an active and stable catalyst for H_2 discharge from H_{12}-MBP at lower temperatures, a mesoporous Pd-Al_2O_3 catalyst (MPdA) was synthesized by a one-pot solvent deficient precipitation (SDP). In the present work, the sensitivity and effectiveness of the SDP method are examined by varying the calcination temperature and time in the preparation of the MPdA catalyst. The characterization revealed that the final properties of the MPdA catalyst greatly rely on both the calcination temperature and time. The MPdA catalyst showed better dehydrogenation activity for calcination at 600 °C than at other temperatures, because of Pd particles of smaller size with higher dispersion. Although the MPdA catalysts calcined at 600 °C for different periods of time have similar size and dispersion of Pd particles, the dehydrogenation efficiency was superior as the calcination time became shorter (e.g., 1 h), which originated from the better arrangement of Pd particles over a higher surface area. These MPdA catalysts, irrespective of the calcination time, displayed a remarkable stability in the dehydrogenation of H_{12}-MBP owing to the protection of Pd particles by the Al_2O_3 layer.

Keywords: dehydrogenation; liquid organic hydrogen carrier; solvent deficient precipitation; mesoporous Pd-Al_2O_3; calcination condition

1. Introduction

Non-renewable fossil fuels represent the major energy sources for current economic development, although they produce large quantities of CO_2 upon combustion, which contribute to global warming. In this regard, a transition to renewable energy is inevitable in order to reduce the dependence on fossil fuels, which will eventually mitigate the energy crisis and alleviate climate change. Hydrogen has been recognized as the most promising renewable and clean energy source for several decades, and it is produced via steam methane reforming and later by renewable energy-powered electrochemical water splitting [1–3]. However, the realization of a viable hydrogen economy is still facing numerous obstacles related to storage and transportation caused by H_2's low volumetric density. Currently, elemental hydrogen is being stored in three different ways: Physical storage, adsorption in materials with high surface areas, and chemical storage [4,5]. Among them, hydrogen storage by means of

chemical bonds is gaining increasing attention. Although solid hydrogen storage materials show high theoretical hydrogen capacity values (e.g., 18.5 wt% for $LiBH_4$), their quantitative uptake and release are highly energy-intensive [1,6–8]. Hence, chemical hydrogen storage using a liquid organic hydrogen carrier (LOHC) has been considered as an alternate viable solution, as these carriers can operate under ambient conditions and have relatively high hydrogen capacity values [4,7].

An LOHC consists of a pair of high boiling-point organic compounds that can undergo reversible hydrogenation and dehydrogenation for the storage and release of hydrogen at elevated temperatures in the presence of a catalyst. The potential benefits of LOHC are good compatibility with the existing fuel infrastructure and the capability to store and transport hydrogen without any losses over long periods under standard conditions [8–11]. Among the different LOHC systems discussed in the literature [4,6,8,9], N-heterocyclic LOHC compounds are considered to be advantageous because of their low dehydrogenation enthalpies, meaning that H_2 release is possible at lower temperatures. Recently, we documented a potential LOHC pair, 2-[(*n*-methylcyclohexyl)methyl]piperidine (H_{12}-MBP) and 2-(*n*-methylbenzyl)pyridine (H_0-MBP), with 6.15 wt% H_2 storage capacity (Scheme 1). Both molecules exist in a liquid state at room temperature (i.e., melting point of H_0-MBP: −50.1 to −46.2 °C and H_{12}-MBP: −19.3 to −18.0 °C) with boiling points of 291–293 °C, clearly fulfilling the thermal requirements for reversible LOHC materials (i.e., having low melting points and high boiling points; in other words, being in liquid state at ambient temperature and also thermally stable at the dehydrogenation temperatures typically above 250 °C) and bearing compatibility with the existing fuel infrastructures [9,12,13]. Although the dehydrogenation of these N-heterocyclic LOHC compounds is thermodynamically favorable, finding an active and stable catalyst to operate at relatively lower temperatures with faster H_2 release is of primary importance for academia and industry.

Scheme 1. Dehydrogenation of 2-[(n-methylcyclohexyl)methyl]piperidine (H_{12}-MBP) to 2-(n-methylbenzyl)pyridine (H_0-MBP).

It is well known that supported Pd catalysts are efficient in the dehydrogenation of N-heterocyclic LOHC compounds; for example, alumina and silica supported Pd catalysts have been successfully applied for the dehydrogenation of dodecahydro-N-ethylcarbazole [14–17], while 5 wt% Pd/Al_2O_3 was used for the dehydrogenation of octahydro-N-ethylindole [18] and octahydro-2-methylindole [19]. Furthermore, Pd/C and Pd/Al_2O_3 catalysts have demonstrated higher H_{12}-MBP dehydrogenation capabilities compared to those of their Pt counter catalysts [12]. However, the Pd/C catalyst fails to retain its dehydrogenation efficiency compared to Pd/Al_2O_3 (showing a slight activity loss) in stability tests because of the accumulation of Pd particles. In the search for stable catalysts, carbon coated Al_2O_3 supported Pd catalysts were considered for the dehydrogenation of H_{12}-MBP and it was noted that a 3.3 wt% carbon coated catalyst exhibited enhanced stability compared to those of other catalysts owing to the control of Pd particle growth by the heterogeneous support surface [13]. Nevertheless, this approach is complex and the final carbon content depends on the textural and acidic properties of the alumina used for the carbon coating. Hence, it is necessary to find an appropriate synthesis method that can produce small Pd particles with higher dispersion and that can maintain Pd particles intact even after repeated dehydrogenation reactions.

Recently, we have developed an amended one-pot solvent deficient precipitation (SDP) for the synthesis of mesoporous $Pd\text{-}Al_2O_3$ (MPdA), which proved to be effective and robust in the dehydrogenation of several N-heterocyclic LOHC compounds including H_{12}-MBP compared to the case of Pd analogs prepared by conventional impregnation [9]. The remarkable performance of the

MPdA catalyst in the dehydrogenation of H_{12}-MBP was caused by highly dispersed Pd particles of smaller sizes, where the stability was enhanced through the inhibition of Pd particle growth by the adjacent Al_2O_3 particles. The unique properties of the MPdA catalyst were shaped by the commencement of a solvent deficient environment in the synthesis, which not only limits the nucleation and growth of nanoparticles, but also introduces the Pd and Al species into the assembly of the mesopore wall. Therefore, the above results encouraged us to further examine the MPdA catalyst by changing the calcination conditions such as temperature and time, which are known to be effective in regulating the physicochemical properties with regard to their dehydrogenation proficiencies [20,21]. Hence, the present work focuses on the investigation of the sensitivity and effectiveness of the SDP method by varying the calcination temperature and calcination time. All MPdA catalysts have been characterized in order to identify the variations affecting the activity and stability in the titled reaction. In consequence, correlations have been drawn between the physicochemical properties and the dehydrogenation activities of MPdA catalysts. Additionally, an optimization study was conducted with the best MPdA catalyst to evaluate whether it can discharge the minimum gravimetric hydrogen storage capacity required for vehicular applications from LOHC.

2. Results and Discussion

2.1. Influence of Calcination Temperature

The SDP method typically involves two steps: Grinding of the reactants and calcination of the resultant intermediate. Therefore, any change in the calcination temperature can modify the final catalyst properties and in turn affect the dehydrogenation capability [20]. Thus, the MPdA catalysts prepared by calcination between 400 °C and 700 °C at intervals of 100 °C were characterized by various techniques.

The textural properties of the calcined MPdA samples were examined by N_2 physisorption (Table 1). All of the samples exhibit type IV isotherms with a hysteresis loop, and confirm the existence of well-developed mesopores. These hysteresis loops, comprised by H2 and H3, indicate the existence of an ink-bottle or channel-like pore connectivity (Figure 1a) and the samples exhibit a relatively narrow pore size distribution (Figure 1b), which agree well with the results of previous reports [9,22]. In detail, the sample calcined at 400 °C (MPdA400_5h) achieved a Brunauer–Emmett–Teller (BET) surface area of 532 $m^2\ g^{-1}$, pore volume of 0.59 $cm^3\ g^{-1}$, and pore size of 3.5 nm. As the calcination temperature increased from 400 °C to 700 °C, the BET surface area continuously decreased (to 282 $m^2\ g^{-1}$) as did the pore volume (to 0.49 $cm^3\ g^{-1}$), while the average pore size increased to 5.2 nm. The declines in the BET surface area and pore volume and increase in the pore size can be explained by the growth of alumina particles. A similar trend was noted in earlier literature [23]. Notably, the capillary condensation shifted toward higher relative pressures as the calcination temperature increased, suggesting an enlargement in the pore size due to development of Al_2O_3 particles. This is consistent with the observations of Zheng et al. [24] and Seo et al. [25].

Table 1. Physicochemical properties of mesoporous Pd-Al_2O_3 (MPdA) catalysts calcined at different temperatures for 5 h.

Catalyst	MPdA400_5h	MPdA500_5h	MPdA600_5h	MPdA700_5h
BET surface area ($m^2\ g^{-1}$)	532 ± 23	418 ± 3	359 ± 1	282 ± 16
Pore volume ($cm^3\ g^{-1}$)	0.59 ± 0.03	0.55 ± 0.01	0.49 ± 0.03	0.49 ± 0.01
Average pore size (nm) [a]	3.5 ± 0.3	3.9 ± 0.3	4.1 ± 0.3	5.2 ± 0.1
Pd particle size (nm) [b]	3.5 ± 0.2	3.4 ± 0.2	2.6 ± 0.1	3.0 ± 0.1
Pd dispersion (%) [b]	32.1 ± 1.8	33.5 ± 2.0	42.4 ± 2.1	37.7 ± 1.9
Pd surface area ($m^2\ g^{-1}$) [b]	143 ± 8	145 ± 9	190 ± 9	169 ± 8
Average Pd particle size (nm) [c]	4.7 ± 0.9	4.5 ± 0.7	3.4 ± 0.5	4.3 ± 0.5
H_2 consumption ($\mu mol\ g^{-1}$) [d]	0.72 ± 0.03	0.69 ± 0.03	0.58 ± 0.02	0.66 ± 0.04

[a] Calculated from the desorption branch; [b] measured by CO chemisorption; [c] estimated from TEM images; [d] Measured by H_2 TPR experiments.

The MPdA samples calcined at different temperatures for 5 h were analyzed by X-ray diffraction (XRD). Figure 1c displays the characteristic peaks of γ-Al_2O_3 (JCPDS #00-029-0063) and PdO (JCPDS #00-043-1024) in all XRD patterns. However, MPdA400_5h displays another diffraction peak, which is related to boehmite (AlOOH) species (JCPDS #00-021-1307), along with the γ-Al_2O_3 and PdO peaks. Smith et al. [26] stated that the boehmite precursor could be transformed to the γ-Al_2O_3 phase below 300 °C; however, the γ-Al_2O_3 at 400 °C still had a substantial amount of boehmite-like stacking-fault defects which gradually disappeared with a rise in calcination temperature. Thus, the presence of boehmite species in MPdA400_5h is inevitable due to the lower calcination temperature, and the absence of diffractions of boehmite species above 400 °C verifies its transformation to the γ-Al_2O_3 phase.

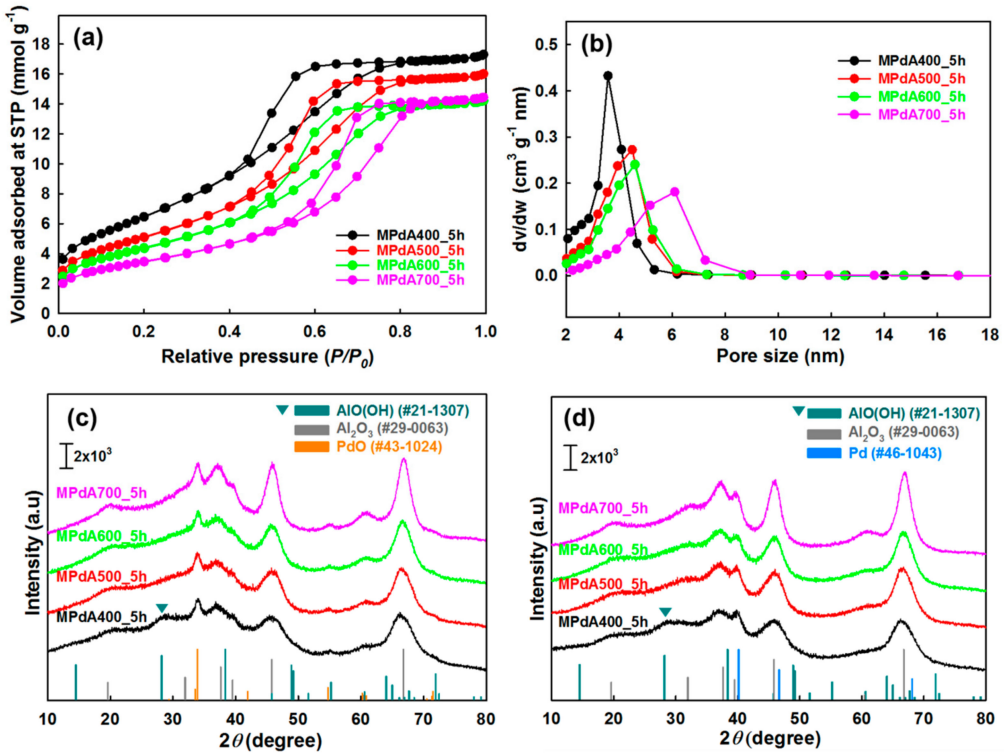

Figure 1. (**a**) Nitrogen adsorption-desorption isotherms; (**b**) pore size distribution curves; (**c**) XRD patterns of the mesoporous Pd-Al_2O_3 (MPdA) catalysts calcined at different temperatures for 5 h; (**d**) XRD patterns of the MPdA catalysts reduced at 350 °C for 3 h; X-ray source: Cu Kα (1.5406 Å).

Furthermore, the increase in the calcination temperature resulted in enlarged reflections of γ-Al_2O_3. This verifies the growth of alumina particles, which will eventually affect the textural properties, such as the decline in BET surface area and pore volume with a corresponding increase in pore size. This was markedly noticed in the N_2 adsorption–desorption results. Although an insignificant change was observed in the intensities of the PdO diffraction peaks, MPdA600_5h among the studied catalysts clearly exhibited low intense PdO diffraction peaks manifesting smaller-size PdO particles. Thus, we examined the XRD patterns of MPdA catalysts reduced at 350 °C for 3 h, which revealed the existence of metallic Pd nanoparticles (JCPDS #00-046-1043) along with the γ-Al_2O_3 visibly presented in Figure 1d. Additionally, a diffraction peak related to boehmite persists in MPdA400_5h, defining that the reduction no longer affects any other species in the calcined catalyst apart from the change of PdO to metallic Pd. However, the diffraction peaks of the metallic Pd nanoparticles in the reduced MPdA catalysts overlap with the diffractions of the support γ-Al_2O_3, introducing a complication in the calculation of Pd particle size using the Scherer equation. Therefore, CO-chemisorption was conducted

instead to determine the Pd particle size along with the Pd dispersion and metal surface area of the reduced MPdA catalysts.

Table 1 shows the Pd dispersion, particle size, and metal surface area of the MPdA catalysts calcined at different temperatures obtained via CO chemisorption after reduction at 350 °C. All catalysts exhibited Pd nanoparticles in the range of 2.6–3.5 nm, even though the calcination temperatures ranging from 400 to 700 °C were considered to be high. Among the studied catalysts, MPdA600_5h yielded the smallest Pd particles (2.6 nm) with higher dispersion (42%) and metal surface area (190 m^2 g^{-1}), while larger Pd particles (3.5 nm) with inferior dispersion (32%) and metal surface area (143 m^2 g^{-1}) were achieved by MPdA400_5h. It is worth mentioning that the particle size of Pd decreased and particle dispersion and metal surface area values increased for the calcination temperature of 600 °C, and a further increase in temperature to 700 °C enhanced the Pd particle size but diminished the particle dispersion and metal surface area. The existence of larger Pd particles with lower dispersion and metal surface areas in MPdA400_5h and MPdA500_5h is quite surprising as compared to the cases of MPdA600_5h and MPdA700_5h.

It is well known that the properties of the support Al_2O_3 always regulate the particle size and dispersions of Pd in Pd/Al_2O_3 catalysts. Byun et al. [20] studied the influence of the calcination temperature on the structural properties of alumina for Pd/Al_2O_3 and found that the size and distribution of Pd particles depend on the phase transition and on the ratio of isolated tetrahedral to condensed octahedral coordination sites. They also reported that the Pd/Al_2O_3 prepared by using Al_2O_3 calcined at 900 °C delivered greater Pd dispersion with smaller size Pd particles compared to those prepared by using Al_2O_3 calcined at 500 °C owing to the presence of higher numbers of isolated tetrahedral sites (AlO_4) than condensed octahedral sites (AlO_6), which have superior interaction capability with Pd. In the present study, all MPdA catalysts were synthesized in a single step by mixing their precursors; hence the distribution and particle sizes of Pd may also depend on the synthesis procedure as well as on the properties of the Al_2O_3. Therefore, the reality of smaller-size Pd particles in all the MPdA catalysts, irrespective of the calcination temperature, may result from the solvent deficient environment generated in the synthesis procedure, which inhibits the migration of reagent materials that would subsequently terminate the nucleation of nanoparticles [27,28]. It was established in our previous study that PdO and γ-Al_2O_3 were the final phases of their precursors (i.e., boehmite (AlOOH) for Al and PdO, $Pd(NH_3)_2(NO_2)_2$, and $(Pd(NO_2)(NH_3)_3)_2(Pd(NH_3)_4(NO_3)_4)$ for Pd) in the MPdA catalyst after calcination [9]. Hence, the interactions between the Al and Pd precursors can decide the distribution and particle size of the Pd, which is ultimately sensitive to the calcination temperature.

Thus, a possible explanation is outlined as follows; the prevalence of larger-size Pd particles in MPdA400_5h can be attributed to the presence of boehmite-like stacking-fault defects, which are clearly perceived in its XRD. The rise in calcination temperature to 500 °C resulted in a trivial difference in the Pd particle size and dispersion. Thus, MPdA500_5h may also have a considerable amount of boehmite-like stacking-fault defects, even though these species were not apparent in its XRD, but were well explained in an earlier report [26]. The realization of smaller-size Pd particles with higher dispersion in MPdA600_5h further confirms the healing of boehmite-like stacking-fault defects and agrees with the observations by Smith et al. [26]. In our tests, a further rise in calcination temperature again produced an increase in particle size with a decrease in dispersion, which was purely related to the aggregation of Pd particles due to exposure to elevated temperatures. These results are well supported by the XRD, where low, intense PdO diffraction peaks in MPdA600_5h are observed among the studied catalysts.

Figure 2 displays the high angle annular dark field scanning transmission electron microscopy (HAADF-STEM) images and particle size distributions of the reduced MPdA catalysts calcined at different temperatures for 5 h, and the average Pd particle sizes are listed in Table 1. All MPdA catalysts revealed that the particles of Pd (bright colored) and Al_2O_3 (grey colored) were stacked fairly tightly, regardless of the calcination temperature. These results agree well with previous literature [22]. Particle size distribution diagrams show that all MPdA catalysts yielded smaller-size Pd particles with

a difference of approximately 1 nm through a significant range in the calcination temperature, owing to the solvent deficient environment, which controls the grain growth of the precipitate and ultimately leads to smaller-size Pd particles. The mean size of the Pd particles in the MPdA catalysts decreased in the following order: MPdA400_5h (4.7 nm) > MPdA500_5h (4.5 nm) > MPdA700_5h (4.3 nm) > MPdA600_5h (3.4 nm). The present findings are in good agreement with the results of the XRD and CO-chemisorption analyses. Furthermore, the TEM images also disclosed an irregular distribution of Pd particles, which can also be clearly observed in their EDS mapping images (not shown here for brevity). It was well documented in our previous study [9] that both palladium and alumina particles are involved in the mesopore formation; therefore, the Pd particles are protected by the Al_2O_3, which limits the migration of Pd particles within the catalyst. This causes the uneven distribution of the Pd particles.

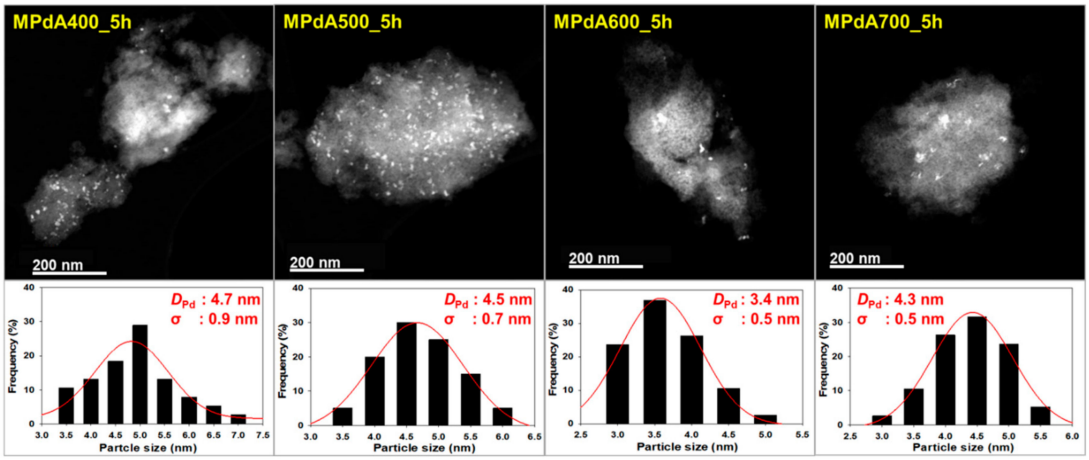

Figure 2. HAADF-STEM images and particle size distributions of the reduced MPdA catalysts calcined at different temperatures for 5 h (D_{Pd}: Pd mean size, σ: standard deviation).

H_2-temperature programmed reduction (H_2-TPR) profiles of the MPdA catalysts calcined at different temperatures for 5 h are shown in Figure 3, and their H_2 consumption values are listed in Table 1. A negative H_2 consumption peak with varying intensity was observed between the Tmax of 103 °C and 113 °C in all MPdA catalysts regardless of calcination temperature. It is well known that the reduction of PdO particles occurs below room temperature, and that they then instantly become a Pd hydride (β-PdH) species by the adsorption/diffusion of hydrogen into the generated metallic Pd crystallites in Pd/Al_2O_3 [29,30]. The formed Pd hydride species later decompose at a higher temperature and exhibit a negative peak. Furthermore, the intensity and position of the negative peak infer the size and dispersion of Pd particles. For instance, larger-size Pd particles have higher H_2 storage capacity, and therefore exhibit higher intense negative peaks, whereas smaller-size Pd particles exhibit low intense negative peaks owing to their lower H_2 storage capacity. Similarly, β-PdH formed by the larger-size Pd particles decomposes at lower temperatures, whereas the β-PdH formed by the smaller-size Pd particles decomposes at higher temperatures [31,32]. Hence, one can confirm that the obtained negative H_2 consumption peak is due to the decomposition of Pd hydrate species formed at ambient temperature (i.e., during the H_2 purge prior to TPR analysis). Among all catalysts tested, MPdA400_5h exhibited the highest intense negative peak at 103 °C, which infers the existence of larger-size Pd particles. In contrast, an increase in the calcination temperature produced a decrease in the negative peak intensity along with a shift in the β-PdH decomposition temperature to higher values, such as 105 °C and 113 °C for MPdA500_5h and MPdA600_5h, respectively. A further increase in the calcination temperature to 700 °C (MPdA700_5h) resulted in a small increase in the intensity of the negative peak along with a slight shift in the β-PdH decomposition temperature to 106 °C. Thus, the outcomes of H_2-TPR endorses that the MPdA600_5h catalyst ensured the lowest intense negative

peak with high temperature β-PdH decomposition among the studied catalysts. This confirms the presence of smaller-size Pd particles in MPdA600_5h. Likewise, the hydrogen consumption values of the MPdA catalysts followed the order: MPdA400_5h (0.72 μmol g^{-1}) > MPdA500_5h (0.69 μmol g^{-1}) > MPdA700_5h (0.66 μmol g^{-1}) > MPdA600_5h (0.58 μmol g^{-1}). The variation in the hydrogen consumption values once again infers the existence of smaller-size Pd particles in MPdA600_5h, while the largest particles are present in MPdA400_5h. The obtained results agree with the conclusions obtained from CO-chemisorption and HAADF-STEM analyses.

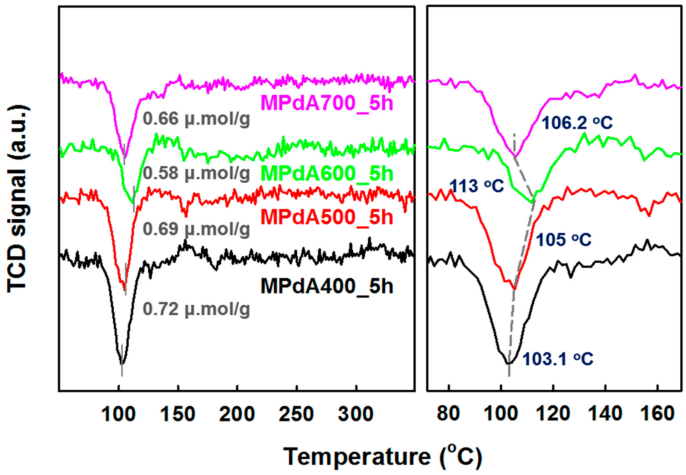

Figure 3. H_2-TPR profiles of the MPdA catalysts calcined at different temperatures for 5 h.

Figure 4a presents the dehydrogenation activity results (obtained by GC analysis) of the MPdA catalysts calcined at different temperatures for 5 h together with their time-dependent H_2 release curves (Figure 4b) at the standard reaction condition used in our previous work (i.e., M/R ratio of 0.1 mol%, 250 °C, and 4 h) [9,12,13]. The time-dependent hydrogen evolution curves reveal that the highest amount of H_2 was released by MPdA600_5h from among the studied catalytic systems. Moreover, MPdA600_5h exhibited the highest first-order rate constant (0.0308 min^{-1} $gcat^{-1}$) and the greatest initial turnover frequency (98.9 cm^{-1}) compared to those of the other calcined catalysts (i.e., MPdA400_5h (0.0067 min^{-1} $gcat^{-1}$, 28.1 cm^{-1}), MPdA500_5h (0.0142 min^{-1} $gcat^{-1}$, 55.0 cm^{-1}) and MPdA700_5h (0.0156 min^{-1} $gcat^{-1}$, 56.4 cm^{-1})), which again confirmed its superior hydrogen liberation capability. It is worth mentioning that the H_2 evolution occurred quickly in the initial period of time and then reached its maximum value within 100 min of the reaction time period. Afterward, the H_2 release plateaued until the end of the reaction for each catalyst. The activity results obtained through the GC also suggested that the H_{12}-MBP conversion, H_0-MBP selectivity, and H_2-yield constantly increased with increasing calcination temperature from 400 °C to 600 °C. MPdA600_5h demonstrated the maximum dehydrogenation capability (i.e., 80% H_{12}-MBP conversion with 75% H_0-MBP selectivity) with uppermost H_2 yield (i.e., 70%). A further rise in temperature to 700 °C (i.e., MPdA700_5h) decreased the H_{12}-MBP conversion to 60% and H_0-MBP selectivity to 67% and accordingly achieved a low yield of H_2 (i.e., 42%). The present results correlate well with the physicochemical properties of MPdA catalysts calcined at different temperatures acquired by the dissimilar characterization techniques we employed.

Figure 5 displays the correlations of Pd dispersion and BET surface area with initial turnover frequency (TOF), calculated by H_2 evolution rate at the initial time of the dehydrogenation reaction (i.e., within 10 min) after reaching the reaction temperature, and final dehydrogenation efficiency calculated from the time-dependent H_2 release curves of MPdA catalysts calcined at different temperatures for 5 h. It is clearly evident that the change in calcination temperature significantly affected the Pd dispersion and BET surface area. It is worth mentioning here that the initial TOF and the final dehydrogenation efficiency of differently calcined MPdA catalysts exhibited a volcano-shaped relationship with the Pd

dispersion. Hence, the acquired results indicate that the higher dispersion of smaller-size Pd particles in MPdA600_5h is responsible for the superior hydrogen release efficiency compared to the case of the other calcined catalysts.

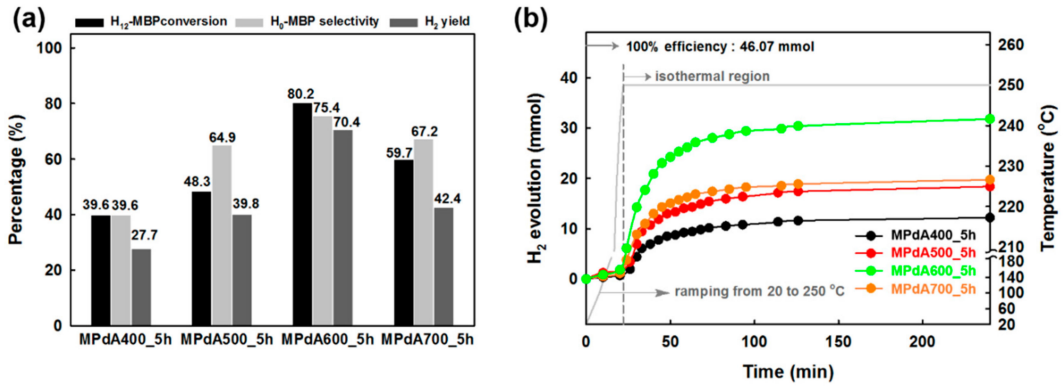

Figure 4. (**a**) Activity results obtained through the GC; (**b**) time-dependent H_2 release curves of the MPdA catalysts calcined at different temperatures for 5 h in the dehydrogenation of H_{12}-MBP at M/R ratio of 0.1 mol% and 250 °C for 4 h.

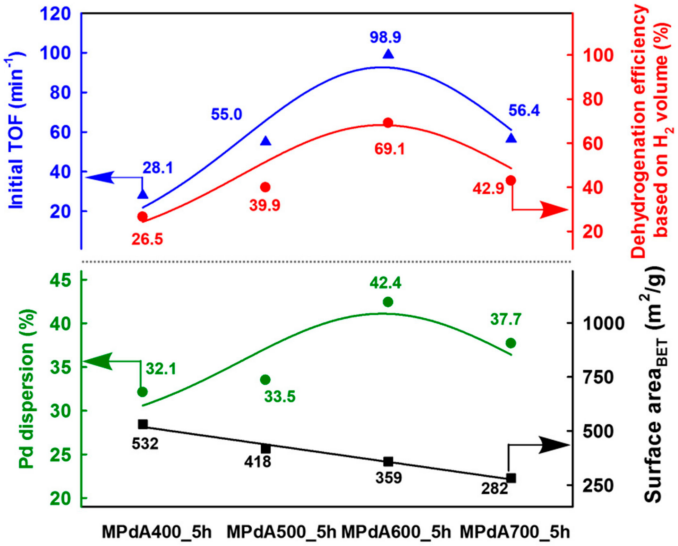

Figure 5. Correlation of Pd dispersion and BET surface area with the initial TOF and the final dehydrogenation efficiency calculated from the time-dependent H_2 release curves of the MPdA catalysts calcined at different temperatures for 5 h.

2.2. *Influence of Calcination Time*

In the SDP method, when the metal nitrate reacts with ammonium bicarbonate, they form a solvent deficient environment which then yields an intermediate hydroxide product (e.g. metal hydroxide or metal oxide hydroxide) and an ammonium nitrate (NH_4NO_3) byproduct [27,28]. During aggregation in the solvent deficient environment, the spectator ions or molecules (NH_4^+, NO_3^-, and H_2O) act as a spatial buffer or form a sort of template around which the agglomerates form and produce mesoporosity after these ions are removed during calcination. In view of this, a minor modification in the calcination process causes a notable improvement in the physicochemical properties of the catalyst. Therefore, we believe that the reduction in calcination time could affect the catalyst properties, which eventually affects their catalytic activity [21]. In the following, the calcination time is changed to 1 h, 3 h, and 5 h for the MPdA catalyst at 600 °C, which was found to yield the best results among the different calcination temperatures tested for H_{12}-MBP dehydrogenation.

Figure 6a shows the dehydrogenation activity results (obtained by GC analyses) of the MPdA catalysts calcined at 600 °C for different calcination durations along with the corresponding time-dependent H_2 release curves (Figure 6b). It is inferred from the time-dependent hydrogen evolution curves that the calcination time does not cause any noteworthy change in the H_2 liberation rate initially, but does cause a notable change at the end of the reaction, following the order: MPdA600_1h > MPdA600_3h > MPdA600_5h. These results were further confirmed by the first-order rate constants and TOFs calculated at the initial time and by the dehydrogenation activity results attained through the GC at the end of the reaction. From these results, the first-order rate constants and TOFs calculated at the initial time using the time-dependent hydrogen release curves indicated negligible changes in the following order: MPdA600_1h (0.0310 min^{-1} $gcat^{-1}$, 101.6 cm^{-1}) ≈ MPdA600_3h (0.0309 min^{-1} $gcat^{-1}$, 101.4 cm^{-1}) ≈ MPdA600_5h (0.0308 min^{-1} $gcat^{-1}$, 98.9 cm^{-1}). However, the dehydrogenation activity results obtained through the GC at the end of the reaction indicated a small variation in the H_{12}-MBP conversion (i.e., approximately 3%), but displayed a substantial improvement in H_0-MBP selectivity and H_2 yield with decreasing calcination time in the ensuing order: MPdA600_5h (H_0-MBP selectivity: 75% and H_2 yield: 70%) < MPdA600_3h (H_0-MBP selectivity: 80% and H_2 yield: 74%) < MPdA600_1h (H_0-MBP selectivity: 83% and H_2 yield: 76%). Thus, it is again confirmed that the change in calcination time has some influence on the dehydrogenation activity. In order to understand the disparities in the catalytic activity, all catalysts were further characterized using different characterization techniques.

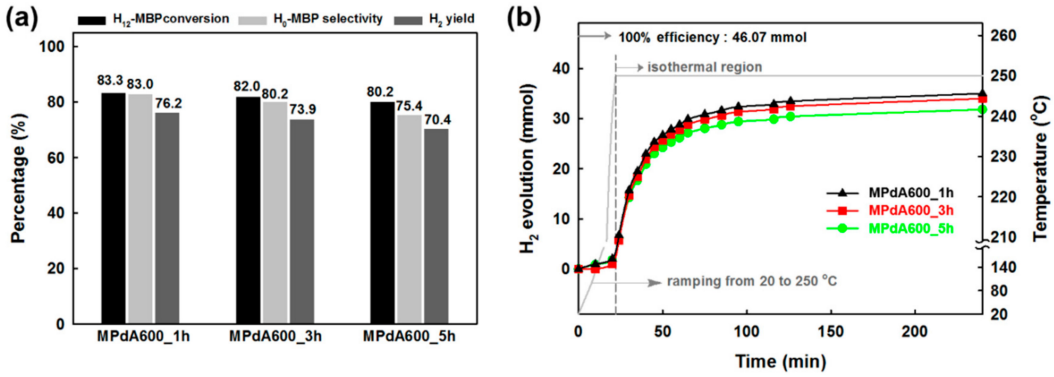

Figure 6. (**a**) Activity results obtained through the GC; (**b**) time-dependent H_2 release curves of the MPdA catalysts calcined at 600 °C for different calcination durations in the dehydrogenation of H_{12}-MBP at M/R ratio of 0.1 mol% and 250 °C for 4 h.

The N_2 physisorption isotherms and pore size distributions of MPdA catalysts calcined at 600 °C for different time intervals are presented in Figure 7a,b, respectively, and the obtained values are summarized in Table 2. All these catalysts show the similar isotherms and hysteresis loops, alike the differently calcined catalysts. Among these catalysts, MPdA600_1h had the highest BET surface area (433 m^2 g^{-1}) and pore volume (0.53 cm^3 g^{-1}), and lowest pore size (3.7 nm). An increase in calcination time to 3 h (MPdA600_3h) substantially decreased the BET surface area (364 m^2 g^{-1}) and pore volume (0.52 cm^3 g^{-1}), and increased the pore size (4.3 nm). A further increase in calcination time to 5 h (MPdA600_5h) resulted in an insignificant difference in the BET surface area (359 m^2 g^{-1}), pore volume (0.49 cm^3 g^{-1}), and pore size (4.1 nm). The hysteresis loops of the MPdA catalysts shifted to higher relative pressures with increasing calcination time, indicating an increase in pore size that can be attributed to dehydroxylation and sintering of alumina particles [25,33]. Therefore, the obtained results indicate that the dehydroxylation and sintering of alumina particles were enormous from 1 h to 3 h, and then nearly stabilized for the 3 h and 5 h calcination times. This explains the significant loss in the BET surface area for MPdA600_3h compared to that for MPdA600_1h and an insignificant difference in BET surface area between MPdA600_5h and MPdA600_3h. The present findings are further confirmed by the following XRD measurements.

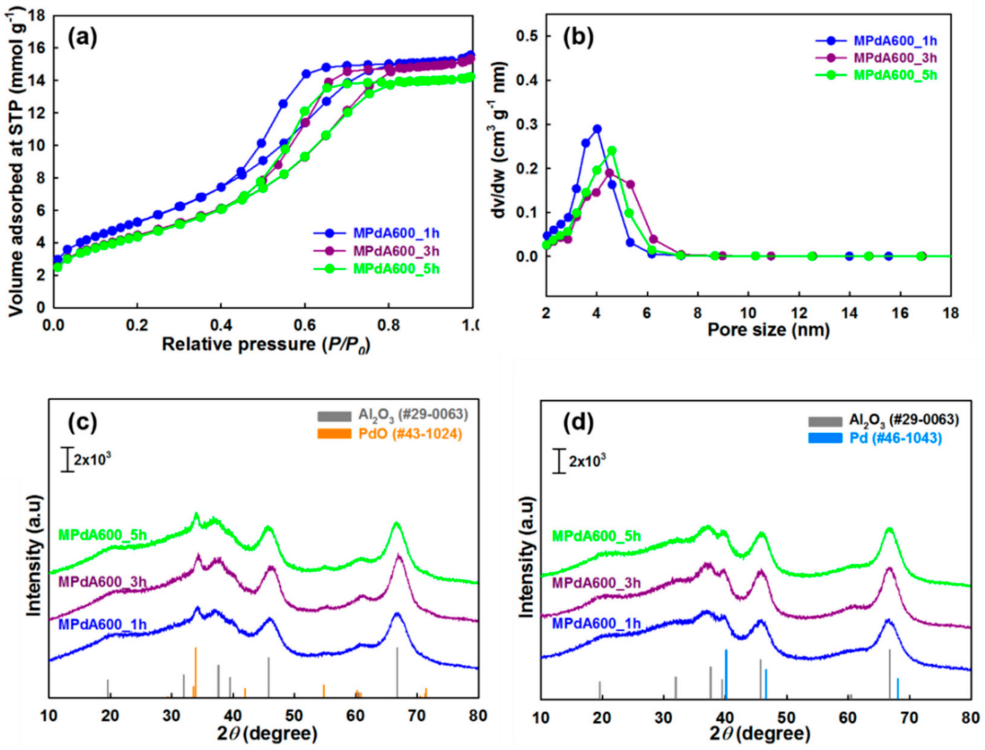

Figure 7. (**a**) Nitrogen adsorption-desorption isotherms; (**b**) pore size distributions; (**c**) XRD patterns of the MPdA catalysts calcined at 600 °C for different durations; (**d**) XRD patterns of the MPdA catalysts reduced at 350 °C for 3 h; X-ray source: Cu Kα (1.5406 Å).

Table 2. Physicochemical properties of the MPdA catalysts calcined at 600 °C for different durations.

Catalyst	MPdA600_1h	MPdA600_3h	MPdA600_5h
BET surface area (m^2 g^{-1})	433 ± 11	364 ± 8	359 ± 1
Pore volume (cm^3 g^{-1})	0.53 ± 0.01	0.52 ± 0.01	0.49 ± 0.03
Average pore size (nm) [a]	3.7 ± 0.3	4.3 ± 0	4.1 ± 0.3
Pd particle size (nm) [b]	2.7 ± 0.1	2.7 ± 0.1	2.6 ± 0.1
Pd dispersion (%) [b]	41.4 ± 1.7	41.5 ± 2.0	42.4 ± 2.1
Pd surface area (m^2 g^{-1}) [b]	185 ± 7	185 ± 9	190 ± 9
Average Pd particle size (nm) [c]	3.4 ± 0.5	3.5 ± 0.6	3.4 ± 0.5
H_2 consumption (μmol g^{-1}) [d]	0.60 ± 0.03	0.61 ± 0.02	0.58 ± 0.02

[a] Calculated from the desorption branch; [b] Measured by CO chemisorption; [c] Estimated from TEM images; [d] Measured by H_2 TPR experiments.

Figure 7c shows the XRD patterns of the MPdA catalysts calcined at 600 °C for different durations. All MPdA catalysts exhibited diffractions of the support γ-Al_2O_3 and the PdO, regardless of the calcination time. The intensity of the diffractions of the support γ-Al_2O_3 noticeably improved with an extension of calcination time from 1 h (MPdA600_1h) to 3 h (MPdA600_3h), verifying the enlargement of alumina particles. Further increase in calcination time to 5 h (MPdA600_5h) revealed negligible evolution in the growth of alumina particles, clearly witnessed from their crystallite sizes i.e., MPdA600_1h (9.7 nm) < MPdA600_3h (10.5 nm) > MPdA600_5h (10.8 nm). These results are in good agreement with the textural properties of MPdA catalysts for different intervals of calcination time, where a drop in BET surface area and pore volume, and an increase in pore size occur as calcination time increases (i.e., major differences in MPdA600_3h compared to MPdA600_1h, and negligible differences between MPdA600_5h and MPdA600_3h). Additionally, delay in the calcination time does not affect the intensities of the PdO diffraction peaks, which validates that all catalysts may have similar-size PdO nanoparticles. Furthermore, the reduced MPdA catalysts revealed the occurrence of

metallic Pd nanoparticles, whose diffraction peaks overlap those of γ-Al_2O_3 (Figure 7d). Therefore, CO chemisorption was employed to determine the Pd particle size along with the Pd dispersion and metal surface area of these catalysts.

The measured CO chemisorption values of the MPdA catalysts calcined at 600 °C with different calcination times after reduction at 350 °C are presented in Table 2. All MPdA catalysts yielded similar Pd dispersions (41–42%) and metal surface areas (185–190 m^2 g^{-1}), as well as similar particle sizes (2.6–2.7 nm). However, the minor differences observed in the CO chemisorption values of MPdA600_1h and MPdA600_3h compared to that of MPdA600_5h can be ascribed to the lower crystallinity of γ-Al_2O_3 achieved by less calcination time, as stated above. The present results suggest that a minor change in the synthesis procedure can regulate final properties of the MPdA catalyst, which verifies the sensitivity and effectiveness of the SDP method. Even a small amendment in the synthesis procedure can cause a considerable variation in catalytic activity (Figure 6).

Figure 8 shows HAADF-STEM images and particle size distributions of the MPdA catalysts calcined at 600 °C for different calcination times after reduction at 350 °C. The average Pd particle sizes are presented in Table 2. In all catalysts Pd and Al_2O_3 particles appeared to be stacked fairly tightly with the similar irregular Pd distributions, as stated before. In particle size distribution diagrams, all catalysts produced smaller-size Pd particles with a negligible difference; i.e., MPdA600_1h (D_{Pd}: 3.4 nm, σ: 0.5 nm), MPdA600_3h (D_{Pd}: 3.5 nm, σ: 0.6 nm), and MPdA600_5h (D_{Pd}: 3.4 nm, σ: 0.5 nm). These are in good agreement with the findings of XRD and CO chemisorption.

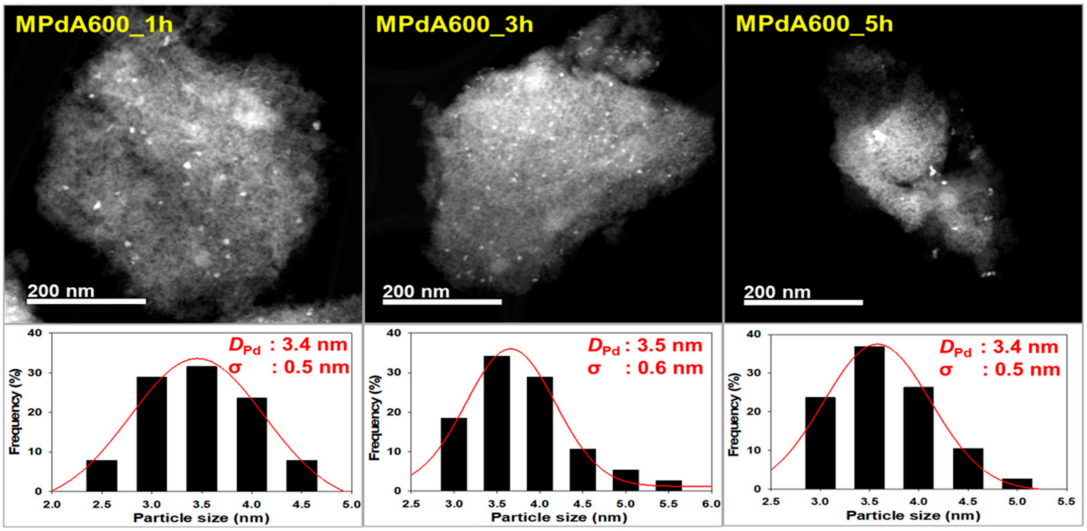

Figure 8. HAADF-STEM images and particle size distributions of the reduced MPdA catalysts calcined at 600 °C for different durations (D_{Pd}: Pd mean size, σ: standard deviation).

H_2-TPR profiles of the MPdA catalysts calcined at 600 °C with variations in calcination time are displayed in Figure 9, and their H_2 consumption values are listed in Table 2. All MPdA catalysts exhibited a negative H_2 consumption peak at T_{max} of 112–113 °C, which could be attributed to the decomposition of Pd hydrate species formed at ambient temperature. In addition, all catalysts exhibited an unimportant change in the negative peak intensity, and achieved similar hydrogen consumption values of 0.58–0.61 μmol g^{-1}. These results again confirmed that a modification in the calcination time does not affect the Pd particle size greatly, which is supported by CO chemisorption results and HAADF-STEM images. These MPdA catalysts exhibited similar characterization results except for the N_2 physisorption results.

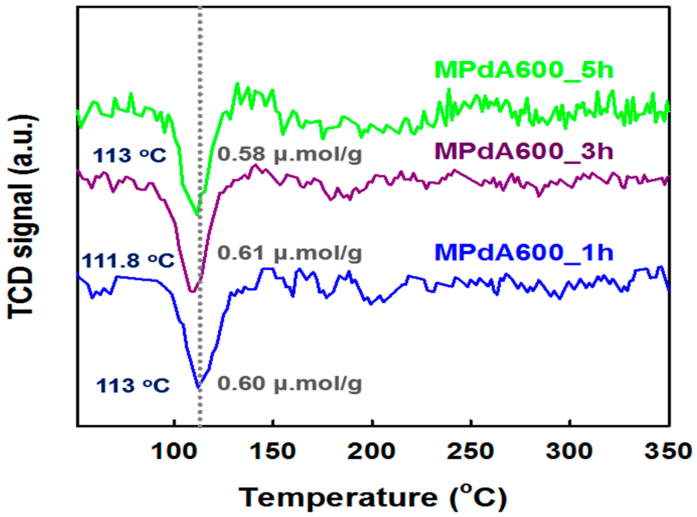

Figure 9. H_2-TPR profiles of the MPdA catalysts calcined at 600 °C for different durations.

Figure 10 displays the correlation of Pd dispersion and BET surface area with the initial TOF and the final dehydrogenation efficiency calculated from the time-dependent H_2 release curves of MPdA catalysts subjected to different calcination durations at 600 °C. It is evident that a change in calcination time affected the BET surface area, but not the Pd dispersion. Interestingly, the change in calcination time does not have any effect at the initial activity but has an effect as time progresses, which can be clearly understood from the results of the initial TOF and the final dehydrogenation efficiency. Hence, the attained results support that a better arrangement of an equal number of active sites exists on the high surface area, which permits the greater hydrogen discharge competence of MPdA600_1h compared to those of MPdA600_3h and MPdA600_5h.

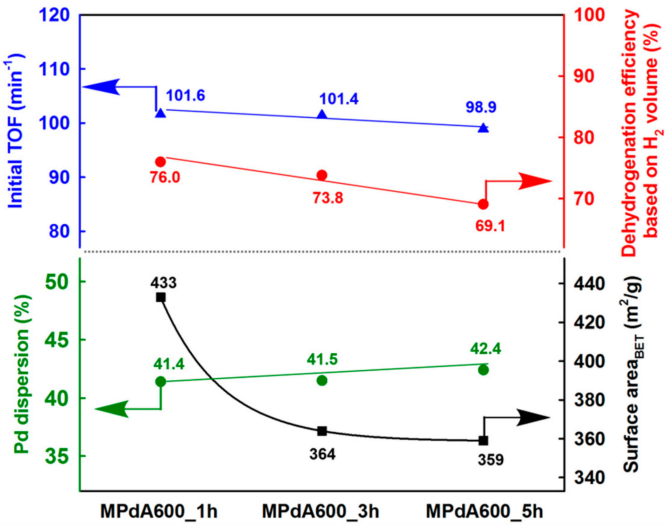

Figure 10. Correlation of the Pd dispersion and BET surface area with the initial TOF and the final dehydrogenation efficiency calculated from the time-dependent H_2 release curves of MPdA catalysts calcined at 600 °C for different calcination durations.

2.3. Optimization of Reaction Parameters

The U.S. Department of Energy (DOE) states that the minimum gravimetric hydrogen storage capacity required for vehicular applications is 5.5 wt% [6,17]. In order to achieve this criterion, optimization of the best catalyst (i.e., MPdA600_1h) is needed. Hence, MPdA600_1h was first tested by changing the M/R ratio from 0.05 mol% to 0.4 mol% at 250 °C for 4 h, and the activity results are presented

in Figure 11a along with their time-dependent H_2 release curves (Figure 11b). The time-dependent H_2 release curves show that the discharge of H_2 increased with such an increase in M/R ratio. The results indicate that the lower discharge of H_2 at the M/R ratio of 0.05 mol% was due to the lower amount of catalyst, while an increase in M/R ratio increased the discharge of H_2, which reached a maximum value of 1076 cm^3 at the M/R ratio of 0.4 mol%. The activity results obtained through the GC also projected the same results, in which an enrichment in H_{12}-MBP conversion, H_0-MBP selectivity, and H_2 yield occurs uninterruptedly as the M/R ratio increases from 0.05 mol% to 0.4%. These results indicate that the use of higher amounts of catalyst (i.e., M/R ratio of 0.4 mol%) assists in the dehydrogenation of both piperidine and the cyclohexane ring in H_{12}-MBP, and harvests approximately 5.8 wt% of H_2 in terms of gravimetric density.

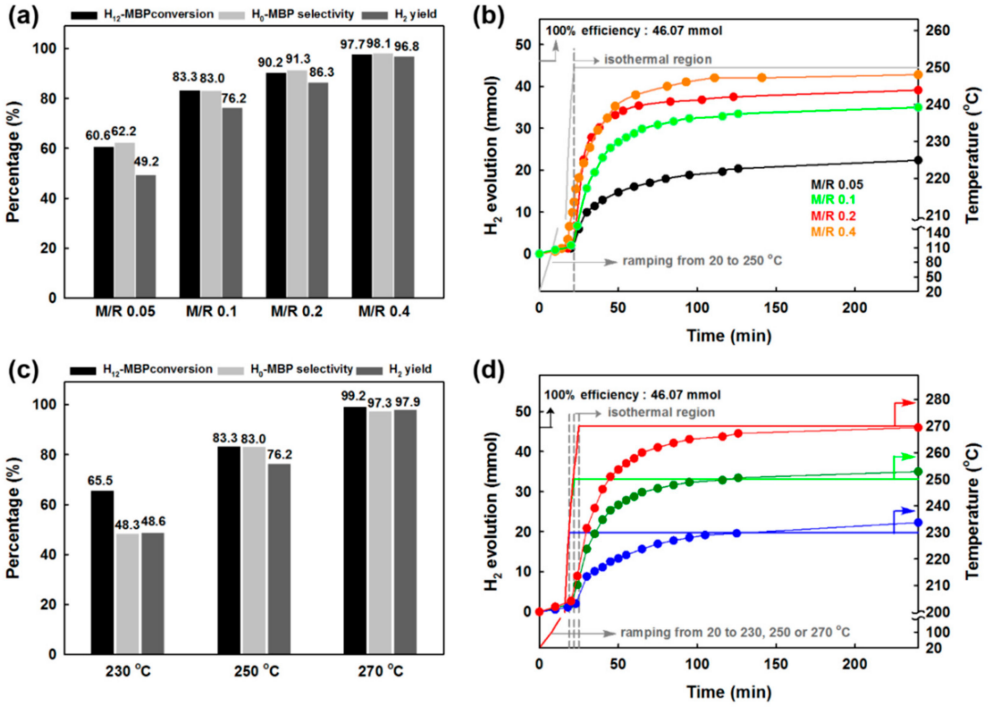

Figure 11. (**a**) Activity results obtained by GC; (**b**) time-dependent H_2 release curves of the MPdA600_1h catalyst with change in M/R ratio at 250 °C and 4 h; (**c**) Activity results obtained through GC; (**d**) time-dependent H_2 release curves of the MPdA600_1h catalyst with change in temperature at M/R ratio of 0.1 mol% and 4 h in the dehydrogenation of H_{12}-MBP.

Later, the dehydrogenation of H_{12}-MBP over MPdA600_1h was examined at various temperatures ranging from 230 °C to 270 °C at 20 °C intervals, and the activity results obtained through the GC are shown in Figure 11c along with their time-dependent H_2 release curves (Figure 11d). It is obvious that the conversion of H_{12}-MBP increases with an increase in reaction temperature. Similarly, H_0-MBP selectivity and H_2 yield also increase with increasing reaction temperature. The obtained low H_0-MBP selectivity and H_2 yield at 230 °C can be explained by the slower dehydrogenation of the cyclohexane ring along with the piperidine ring in H_{12}-MBP. It can be expected that a rise in reaction temperature enables a more pronounced dehydrogenation of the cyclohexane ring in H_{12}-MBP, and thus aids in achieving higher H_0-MBP selectivity and H_2 yield (which is equivalent to 6.1 wt% of H_2 gravimetric density). Hence, the results indicate that the minimum required amount of H_2 for mobile applications (i.e., 5.5 wt%) can be attained either by increasing the temperature to 270 °C at 0.1 mol% M/R or by increasing the M/R ratio to 0.4 mol% at 250 °C.

2.4. Catalyst Stability

The MPdA catalysts with different calcination durations were evaluated regarding their stability at 250 °C for 4 h using an M/R ratio of 0.1 mol% in five repeated cycles (Figure 12). This reaction condition was purposefully selected to show a notable difference in their dehydrogenation capabilities. Surprisingly, all MPdA catalysts exhibited outstanding stability in all five runs, which is attributed to the maintenance of smaller-size Pd particles (i.e., MPdA600_1h (3.6 nm) ≈ MPdA600_3h (3.8 nm) ≈ MPdA600_5h (3.9 nm)), and further witnessed from HAADF-STEM images taken after five runs (not shown here for brevity).

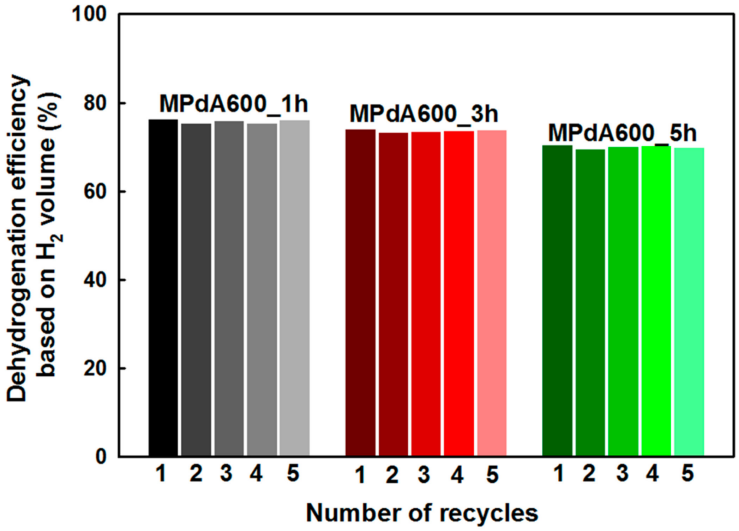

Figure 12. Recyclability of the MPdA catalysts calcined at 600 °C for different periods in the dehydrogenation of H_{12}-MBP at M/R of 0.1 mol% and 250 °C for 4 h.

In addition, the high-resolution TEM (HRTEM) images (Figure 13) of fresh and spent MPdA catalysts revealed that the Pd particles are shielded by the Al_2O_3 layer. Hence, it is likely that this protection mechanism prevents the mobility of Pd particles during the course of reaction and also constrains their aggregation, therefore preserving the dehydrogenation capability over successive cycles. It was well established in our previous study that both Pd and Al_2O_3 particles are involved in the construction of the mesopore wall and hence the protection of Pd particles by Al_2O_3 is apparent in the HRTEM images. Thus, the present results reinforced the earlier observation. Moreover, all fresh and spent MPdA catalysts exhibited only the Pd(111) facets, irrespective of the calcination time. Therefore, the present results again establish that the SDP method is unambiguous in generating Pd(111) facets, which were found to be the dominant active sites for the dehydrogenation reaction because of the inherent close-packed structure [9,14,16,34,35].

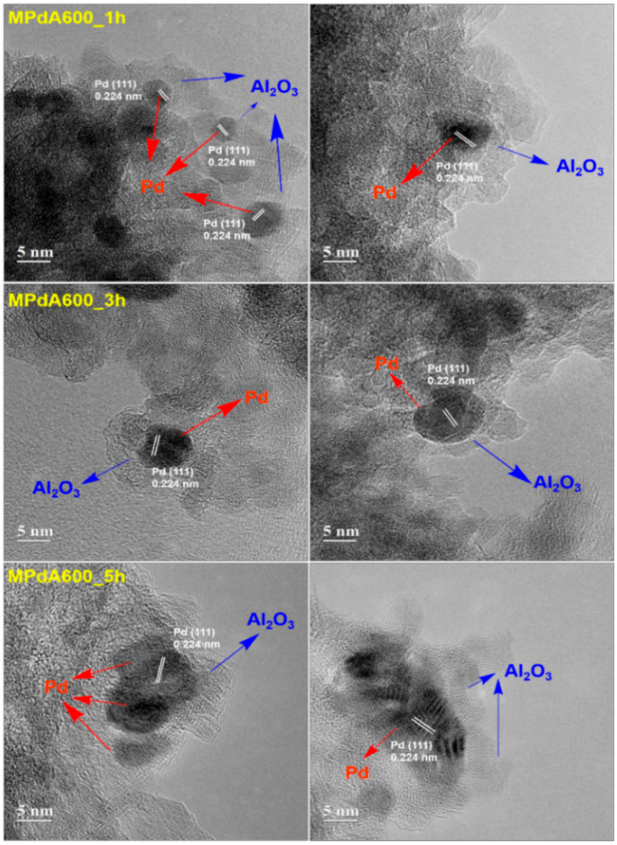

Figure 13. HRTEM images of MPdA catalysts calcined at 600 °C for different periods of time: left images show fresh samples and right images show spent samples.

3. Materials and Methods

3.1. Preparation of Mesoporous 1 wt% Pd-Al_2O_3

An amended SDP method was used for the synthesis of mesoporous 1 wt% Pd-Al_2O_3 described in our previous work [9]. In a typical synthesis, the calculated amounts of palladium nitrate ($Pd(NO_3)_2{\cdot}H_2O$), aluminum nitrate ($Al(NO_3)_3{\cdot}9H_2O$), and ammonium bicarbonate (NH_4HCO_3) with a molar metal-to-bicarbonate ratio of 1:3 were mixed in a mortar and were ground thoroughly by a pestle at room temperature for 20 min, which released not only liquid water but also CO_2 bubbles from the reacting salts. The grinding continued until precipitation of Pd and Al was completed, which was evidenced by no further CO_2 formation. The resulting precursor was calcined at different temperatures (400, 500, 600, or 700 °C) for 5 h with a ramping rate of 2 °C min^{-1}, followed by an identical H_2 reduction at 350 °C for 3 h with a ramping rate of 5 °C min^{-1}. In the calcination step, the lower ramping rate was used to avoid rapid dehydration in order to ensure uniform pore development and uniform heat transfer that avoids rapid grain growth and attains better homogeneity. After an optimal calcination temperature was selected, the calcination time (duration) was varied as 5 h, 3 h, and 1 h. The prepared catalyst is designated as MPdAX_Y, where X and Y indicate the calcination temperature and time, respectively. For instance, MPdA600_5h represents the mesoporous 1 wt% Pd-Al_2O_3 (MPdA) prepared by calcination at 600 °C for 5 h.

3.2. Catalyst Characterization

The Brunauer–Emmett–Teller (BET) surface area and pore size distribution were measured using a Micromeritics ASAP 2010 system (Norcross, GA, USA) after pretreatment at 200 °C for 2 h under vacuum. X-ray diffraction (XRD) analysis was conducted with a Rigaku miniFlex300 diffractometer

(Spring, TX, USA) using a Cu Kα (1.5406 Å) radiation source (30 kV and 10 mA), where all patterns were recorded at a scan rate of 4° min^{-1} with a step of 0.02°. The crystallite sizes of the support were calculated using the Debye–Scherrer equation ($K\lambda/\beta cos\theta$). CO chemisorption was carried out with a BELCAT-B instrument (BEL Japan, Inc.) for the measurement of Pd particle sizes. After the calcined sample (50 mg) was reduced at 350 °C for 3 h in a 10% H_2/Ar flow and then cooled to 30 °C by He flow, a pulse of 5% CO/He gas was repeatedly injected until the peak area became saturated. The amount of CO chemisorbed was determined from the integrated peak areas, and by comparing them with that of the calibrated area obtained from a 100 ml sample of the adsorbing gas mixture injected through a sample loop. The CO-to-Pd ratio of 1:1 was used to calculate the Pd dispersion, and a spherical geometry of Pd crystallites was assumed when calculating the average particle diameter from the data of the CO uptake. Images of high angle annular dark field scanning transmission electron microscopy (HAADF-STEM) and high-resolution TEM (HRTEM), and atomic mapping were taken using a JEOL JEM-2100F microscope (Tokyo, Japan) with an acceleration voltage of 200 kV, where a specimen was prepared by dropping a catalyst sample in methanol onto a copper grid and subsequently vacuum drying it at 60 °C. H_2 temperature-programmed reduction (H_2-TPR) experiments were carried out on a Micromeritics AutoChemII 2910 instrument (Norcross, GA, USA), where a calcined MPdA sample (60 mg) was pre-treated under Ar flow at 500 °C for 1 h and then cooled to room temperature. Later, the amount of H_2 consumption was measured by a thermal conductivity detector as the temperature was increased to 800 °C at 10 °C min^{-1} in a 10% H_2/Ar flow.

3.3. Dehydrogenation of 2-[(n-methylcyclohexyl)methyl]Piperidine (H_{12}-MBP)

The reduced MPdA catalyst was tested for the dehydrogenation of H_{12}-MBP in a batch reactor (volume: 90 cm^3) described previously [9,12,13]. In a typical experiment, H_{12}-MBP of 7.3 mmol was added dropwise to the MPdA catalyst pre-loaded at the bottom of the reactor vessel, where the catalyst weight was varied to obtain a desired metal-to-reactant (M/R) ratio. Prior to each reaction, the reactor was purged with N_2 for 10 min to remove inner moisture and oxygen. Then, the reaction mixture was heated at 18 °C min^{-1} to a desired temperature using a commercial heat-transfer fluid, followed by the dehydrogenation reaction conducted for a desired period of time. The volume of H_2 released during the reaction was monitored by the water volume displaced in a glass burette and measured with an accuracy of ±2 cm^3 (examined by repeating the experiment at least three times under identical conditions). After the completion of the reaction, the reactor was cooled to ambient temperature and the reaction mixture was diluted with acetone (20 cm^3) and filtered via a syringe filter (0.1 μm). An aliquot of this solution was mixed with a gas chromatograph (GC) calibration solvent nonane and then analyzed with a Youngling YL6500 GC equipped with a flame ionization detector (FID) and a HP-5 column (30 m × 0.32 mm× 0.25 μm). More detailed GC analysis was performed in an Agilent Technologies 7890A GC equipped with an auto sampler (7683D), a FID, and a Restek Rxi®-17Sil column (30 m × 0.25 mm × 0.25 μm). Furthermore, close examination of gas products revealed the absence of other gas formations, confirming the high purity of hydrogen, while the nonappearance of ring opening products in the liquid phase indicated the stability of the LOHC material under the current reaction conditions.

For quantification, H_{12}-MBP conversion (Equation (1)), H_0-MBP selectivity (Equation (2)), and H_2 yield (Equation (3)) were calculated from the GC results, while dehydrogenation efficiency (Equation (4)) was based on H_2 volume measured by the gas burette, as follows:

$$\text{H_{12}-MBP conversion (mol\%)} = (\text{initial H_{12}-MBP [mol]} - \text{final H_{12}-MBP [mol]})/(\text{initial H_{12}-MBP [mol]}) \times 100\% \quad (1)$$

$$\text{H_0-MBP selectivity (mol\%)} = (\text{final H_0-MBP [mol]})/(\text{final H_0-MBP [mol]} + \text{final H_6-MBP [mol]}) \times 100\% \quad (2)$$

$$H_2 \text{ yield (mol\%)} = \{(\text{final } H_6\text{-MBP [mol]} \times 3H_2) + (\text{final } H_0\text{-MBP [mol]} \times 6H_2)\}/(\text{initial } H_{12}\text{-MBP [mol]} \times 6H_2) \times 100\% \quad (3)$$

$$\text{Dehydrogenation efficiency (\%)} = (\text{measured gas volume [cm}^3\text{]})/(\text{initial } H_{12}\text{-MBP [mol]} \times 82\ [\text{cm}^3\ \text{mol}^{-1}\ \text{K}^{-1}] \times 298.\ 15\ [\text{K}]) \times 100\% \quad (4)$$

3.4. Catalyst Recyclability Tests

The catalyst sample that was recovered after a reaction was washed three times with a mixture of acetone and heptane and dried at 105 °C in an oven. As a final step, the sample was reduced by H_2 at 350 °C for 3 h. This procedure was repeated after each reaction run.

4. Conclusions

Mesoporous Pd-Al_2O_3 (MPdA) catalysts synthesized by an amended one-pot solvent deficient precipitation (SDP) are found to be active and selective for the dehydrogenation of a potential LOHC (i.e., H_{12}-MBP). Both the calcination temperature and time have a strong influence on the final physicochemical properties of MPdA catalysts. The realization of smaller size Pd particles in all MPdA catalysts irrespective of their calcination temperature and time can be attributed to the solvent deficient environment generated in the synthesis procedure, which inhibits the migration of reagent materials that subsequently would prevent the nucleation of the nanoparticles. The characterization studies of MPdA catalysts calcined at different temperatures reveal that the healing of boehmite-like stacking-fault defects is responsible for the existence of smaller Pd particles with higher dispersion in MPdA600_5h, resulting in its better dehydrogenation capability compared to the other studied catalysts. In contrast, a change in the calcination time does not affect the Pd particle size and dispersion, but does affect the BET surface area. The greater dehydrogenation efficiency achieved by MPdA600_1h results from the superior arrangement of the same number of active sites on a higher surface area. The optimization studies indicate that the amount of H_2 required for mobile applications (i.e., 5.5 wt%) can be achieved either by increasing the temperature to 270 °C at 0.1 mol% M/R or by increasing the M/R ratio to 0.4 mol% at 250 °C. Furthermore, the exceptional stability of MPdA catalysts in the dehydrogenation of H_{12}-MBP is realized because the Al_2O_3 limited the Pd particle growth. Finally, the present work introduces a cost-effective and facile synthesis route for the preparation of stable mesoporous Pd-Al_2O_3 catalysts.

Author Contributions: Data curation, H.B.B.; conceptualization, H.B.B. and Y.-W.S.; methodology, H.B.B.; validation, H.B.B., J.O., Y.J., and Y.-W.S.; investigation, H.B.B., J.O., and Y.J. (H.B.B.: material design, synthesis, and catalyst characterization, J.O.: catalyst characterization and catalytic experiments, Y.J.: catalytic experiments); visualization, H.B.B. and Y.-W.S.; supervision, Y.-W.S.; writing—original draft preparation, H.B.B.; writing—review and editing, H.B.B. and Y.-W.S.; project administration, Y.-W.S.; funding acquisition, Y.-W.S.

Funding: This work was financially supported by the Korea Institute of Energy Technology Evaluation and Planning funded by the Ministry of Trade, Industry & Energy, Republic of Korea (KETEP-20173030041360) and by the National Research Foundation of Korea (NRF) funded by the Ministry of Science and ICT, Republic of Korea (NRF-2019M3E6A1064908). H.B.B. acknowledges the financial support by the Basic Science Research Program through the NRF through funded by the Ministry of Education, Republic of Korea (NRF-2016R1A6A1A03013422).

Conflicts of Interest: The authors declare no conflict of interest.

References

1. Zhong, H.; Iguchi, M.; Chatterjee, M.; Himeda, Y.; Xu, Q.; Kawanami, H. Formic acid-based liquid organic hydrogen carrier system with heterogeneous catalysts. *Adv. Sustainable Syst.* **2018**, 1700161. [CrossRef]
2. Bourane, A.; Elanany, M.; Pham, T.V.; Katikaneni, S.P. An overview of organic liquid phase hydrogen carriers. *Int. J. Hydrogen Energy.* **2016**, *41*, 23075–23091. [CrossRef]
3. Liu, K.H.; Zhong, H.X.; Li, S.J.; Duan, Y.X.; Shi, M.M.; Zhang, X.B.; Yan, J.M.; Jiang, Q. Advanced catalysts for sustainable hydrogen generation and storage via hydrogen evolution and carbon dioxide/nitrogen reduction reactions. *Prog. Mater. Sci.* **2018**, *92*, 64–111. [CrossRef]

4. Gianotti, E.; Jacquin, M.T.; Rozière, J.; Jones, D.J. High-purity hydrogen generation via dehydrogenation of organic carriers: A review on the catalytic process. *ACS Catal.* **2018**, *8*, 4660–4680. [CrossRef]
5. Ren, J.; Musyoka, N.M.; Langmi, H.W.; Mathe, M.; Liao, S. Current research trends and perspectives on materials-based hydrogen storage solutions: A critical review. *Int. J. Hydrogen Energy* **2017**, *42*, 289–311. [CrossRef]
6. Zhu, Q.L.; Xu, Q. Liquid organic and inorganic chemical hydrides for high-capacity hydrogen storage. *Energy Environ. Sci.* **2015**, *8*, 478–512. [CrossRef]
7. Crabtree, R.H. Hydrogen storage in liquid organic heterocycles. *Energy Environ. Sci.* **2008**, *1*, 134–138. [CrossRef]
8. Saksa, P.T.A.; Cook, C.; Kiviaho, J.; Repo, T. Liquid organic hydrogen carriers for transportation and storing of renewable energy—Review and discussion. *J. Power Sources* **2018**, *396*, 803–823. [CrossRef]
9. Oh, J.; Bathula, H.B.; Park, J.H.; Suh, Y.W. A sustainable mesoporous palladium-alumina catalyst for efficient hydrogen release from N-heterocyclic liquid organic hydrogen carriers. *Commun. Chem.* **2019**, *2*, 68. [CrossRef]
10. Amende, M.; Gleichweit, C.; Werner, K.; Schernich, S.; Zhao, W.; Lorenz, M.P.A.; Hofert, O.; Papp, C.; Koch, M.; Wasserscheid, P.; et al. Model catalytic studies of liquid organic hydrogen carriers: Dehydrogenation and decomposition mechanisms of dodecahydro-N-ethylcarbazole on Pt(111). *ACS Catal.* **2014**, *4*, 657–665. [CrossRef]
11. Do, G.; Preuster, P.; Aslam, R.; Bösmann, A.; Müller, K.; Arlt, W.; Wasserscheid, P. Hydrogenation of the liquid organic hydrogen carrier compound dibenzyltoluene—Reaction pathway determination by ^{1}H NMR spectroscopy. *React. Chem. Eng.* **2016**, *1*, 313–320. [CrossRef]
12. Oh, J.; Jeong, K.; Kim, T.W.; Kwon, H.; Han, J.W.; Park, J.H.; Suh, Y.W. 2-(N-Methylbenzyl)pyridine: A potential liquid organic hydrogen carrier with fast H_2 release and stable activity in consecutive cycles. *ChemSusChem* **2018**, *11*, 661–665. [CrossRef]
13. Oh, J.; Kim, T.W.; Jeong, K.; Park, J.H.; Suh, Y.W. Enhanced activity and stability of a carbon-coated alumina-supported Pd catalyst in the dehydrogenation of a liquid organic hydrogen carrier, perhydro 2-(n-methylbenzyl)pyridine. *ChemCatChem* **2018**, *10*, 3892–3900. [CrossRef]
14. Sobota, M.; Nikiforidis, I.; Amende, M.; Zanon, B.S.; Staudt, T.; Hofert, O.; Lykhach, Y.; Papp, C.; Hieringer, W.; Laurin, M.; et al. Dehydrogenation of dodecahydro-N-ethylcarbazole on Pd/Al_2O_3 model catalysts. *Chem. Eur. J.* **2011**, *17*, 11542–11552. [CrossRef]
15. Yang, M.; Dong, Y.; Fei, S.; Ke, H.; Cheng, H. A comparative study of catalytic dehydrogenation of perhydro-N-ethylcarbazole over noble metal catalysts. *Int. J. Hydrogen Energy* **2014**, *39*, 18976–18983. [CrossRef]
16. Sotoodeh, F.; Smith, K.J. Structure sensitivity of dodecahydro-N-ethylcarbazole dehydrogenation over Pd catalysts. *J. Catal.* **2011**, *279*, 36–47. [CrossRef]
17. Sotoodeh, F.; Zhao, L.; Smith, K.J. Kinetics of H_2 recovery from dodecahydro-N-ethylcarbazole over a supported Pd catalyst. *Appl. Catal. A* **2009**, *362*, 155–162. [CrossRef]
18. Dong, Y.; Yang, M.; Yang, Z.; Ke, H.; Cheng, H. Catalytic hydrogenation and dehydrogenation of N-ethylindole as a new heteroaromatic liquid organic hydrogen carrier. *Int. J. Hydrogen Energy* **2015**, *40*, 10918–10922. [CrossRef]
19. Li, L.; Yang, M.; Dong, Y.; Mei, P.; Cheng, H. Hydrogen storage and release from a new promising liquid organic hydrogen storage carrier (LOHC): 2-methylindole. *Int. J. Hydrogen Energy* **2016**, *41*, 16129–16134. [CrossRef]
20. Byun, M.Y.; Kim, J.S.; Park, D.W.; Lee, M.S. Influence of calcination temperature on the structure and properties of Al_2O_3 as support for Pd catalyst. *Korean J. Chem. Eng.* **2018**, *35*, 1083–1088. [CrossRef]
21. Dey, S.; Dhal, G.C.; Mohan, D.; Prasad, R. Effect of preparation conditions on the catalytic activity of CuMnOx catalysts for CO oxidation. *Bull. Chem. React. Eng. Catal.* **2017**, *12*, 437–451. [CrossRef]
22. Huang, B.; Bartholomew, C.H.; Smith, S.J.; Woodfield, B.F. Facile solvent-deficient synthesis of mesoporous γ-alumina with controlled pore structures. *Micro. Meso. Mater.* **2013**, *165*, 70–78. [CrossRef]
23. Chen, X.; Zheng, Y.; Huang, F.; Xiao, Y.; Cai, G.; Zhang, Y.; Zheng, Y.; Jiang, L. Catalytic activity and stability over nanorod-like ordered mesoporous phosphorus-doped alumina supported palladium catalysts for methane combustion. *ACS Catal.* **2018**, *8*, 11016–11028. [CrossRef]

24. Zheng, X.; Chen, X.; Chen, J.; Zheng, Y.; Jiang, L. Synthesis and application of highly dispersed ordered mesoporous silicon-doped Pd-alumina catalyst with high thermal stability. *Chem. Eng. J.* **2016**, *297*, 148–157. [CrossRef]
25. Seo, J.G.; Youn, M.H.; Park, S.; Chung, J.S.; Song, I.K. Hydrogen production by steam reforming of liquefied natural gas (LNG) over Ni/Al_2O_3–ZrO_2 xerogel catalysts: Effect of calcination temperature of Al_2O_3–ZrO_2 xerogel supports. *Int. J. Hydrogen Energy* **2009**, *34*, 3755–3763. [CrossRef]
26. Smith, S.J.; Amin, S.; Woodfield, B.F.; Goates, J.B.; Campbell, B.J. Phase progression of γ-Al_2O_3 nanoparticles synthesized in a solvent-deficient environment. *Inorg. Chem.* **2013**, *52*, 4411–4423. [CrossRef]
27. Smith, S.J.; Huang, B.; Liu, S.; Liu, Q.; Olsen, R.E.; Goates, J.B.; Woodfield, B.F. Synthesis of metal oxide nanoparticles via a robust "solvent-deficient" method. *Nanoscale* **2015**, *7*, 144–156. [CrossRef]
28. Brunner, K.M.; Huang, B.; Woodfield, B.F.; Hecker, W.C. Iron fischer-tropsch catalysts prepared by solvent-deficient precipitation (SDP): Effects of washing, promoter addition step, and drying temperature. *Catalysts* **2015**, *5*, 1352–1374. [CrossRef]
29. Esteves, L.M.; Brijaldo, M.H.; Passos, F.B. Decomposition of acetic acid for hydrogen production over Pd/Al_2O_3 and Pd/TiO_2: Influence of metal precursor. *J. Mol. Catal. A Chem.* **2016**, *422*, 275–288. [CrossRef]
30. Gil, S.; Vargas, J.M.G.; Liotta, L.F.; Pantaleo, G.; Ousmane, M.; Retailleau, L.; Fendler, A.G. Catalytic oxidation of propene over Pd catalysts supported on CeO_2, TiO_2, Al_2O_3 and M/Al_2O_3 Oxides (M = Ce, Ti, Fe, Mn). *Catalysts* **2015**, *5*, 671–689. [CrossRef]
31. Bhogeswararao, S.; Srinivas, D. Catalytic conversion of furfural to industrial chemicals over supported Pt and Pd catalysts. *J. Catal.* **2015**, *327*, 65–77. [CrossRef]
32. Zheng, Q.; Farrauto, R.; Deeba, M. Part II: Oxidative thermal aging of Pd/Al_2O_3 and Pd/Ce_xO_y-ZrO_2 in automotive three way catalysts: The effects of fuel shutoff and attempted fuel rich regeneration. *Catalysts* **2015**, *5*, 1797–1814. [CrossRef]
33. Sun, Z.X.; Zheng, T.T.; Bo, Q.B.; Du, M.; Forsling, W. Effects of calcination temperature on the pore size and wall crystalline structure of mesoporous alumina. *J. Colloid Interface Sci.* **2008**, *319*, 247–251. [CrossRef]
34. Sotoodeh, F.; Smith, K.J. Analysis of H_2 release from organic polycyclics over Pd catalysts using DFT. *J. Phys. Chem. C* **2013**, *117*, 194–204. [CrossRef]
35. Amende, M.; Schernich, S.; Sobota, M.; Nikiforidis, I.; Hieringer, W.; Assenbaum, D.; Gleichweit, C.; Drescher, H.J.; Papp, C.; Steinruck, H.P.; et al. Dehydrogenation mechanism of liquid organic hydrogen carriers: Dodecahydro-N-ethylcarbazole on Pd(111). *Chem. Eur. J.* **2013**, *19*, 10854–10865. [CrossRef]